

Supplementary material: The interplay of activity and filament flexibility determines the emergent properties of active nematics

Abhijeet Joshi, Elias Putzig, Aparna Baskaran, and Michael F. Hagan
Martin Fisher school of physics, Brandeis University, Waltham, MA 02453, USA

(Dated: October 28, 2018)

CONTENTS

S1. Simulation movies	1
S2. Analysis	1
S3. Additional figures on scaling of active nematic characteristics with κ_{eff}	2
S4. Estimating the individual filament persistence length	2
S5. Splay and bend deformations	3
S6. System size effects	4
S7. Density fluctuations	5
S8. Defect identification and shape measurement algorithm	6
References	8

S1. SIMULATION MOVIES

Animations of simulation trajectories (showing 1/16 of the simulation box) are provided for the following parameter sets, with $k_b = 300$ and $\tau_1 = 0.2$ in all cases:

- fa5_k500_t0p2.mp4: $\kappa_{\text{eff}} = 20 : \kappa = 500, f^a = 5$
- fa5_k2500_t0p2.mp4: $\kappa_{\text{eff}} = 100 : \kappa = 2500, f^a = 5$
- fa10_k200_t0p2.mp4: $\kappa_{\text{eff}} = 2 : \kappa = 200, f^a = 10$
- fa10_k2500_t0p2.mp4: $\kappa_{\text{eff}} = 25 : \kappa = 2500, f^a = 10$
- fa30_k10000_t0p2.mp4: $\kappa_{\text{eff}} = 11 : \kappa = 10^4, f^a = 30$

In the videos, white arrows indicate positions and orientations of $+\frac{1}{2}$ defects and white dots indicate positions of $-\frac{1}{2}$ defects. Filament beads are colored according to the orientations of the local tangent vector.

S2. ANALYSIS

To analyze our simulation trajectories within the framework of liquid crystal theory, we calculated the local nematic tensor as $Q_{\alpha\beta}(r_{ij}) = \sum_{k, |r_k - r_{ij}| < 5\sigma} (\hat{t}_{k\alpha}\hat{t}_{k\beta} - \frac{1}{2}\delta_{\alpha\beta})$ and the density field ρ on a 1000×1000 grid, where, r_{ij} is the position of the grid point and r_k and t_k are the positions and tangent vectors of all segments. We then evaluated the local nematic order parameter, S and director \hat{n} as the largest eigenvalue of Q and corresponding eigenvector. We identified defects in the director field and their topological charges using the procedure described in section S8. To compare the magnitudes of splay and bend deformations in our active systems to those that occur at equilibrium, we calculated elastic constants of our system at equilibrium ($f^a = 0$) using the free energy perturbation technique proposed by Joshi et al. [1]. We performed these equilibrium calculations on a box of size $64 \times 64\sigma^2$.

S3. ADDITIONAL FIGURES ON SCALING OF ACTIVE NEMATIC CHARACTERISTICS WITH κ_{eff}

We present data on defect density from the alternative data set in Fig. S1.

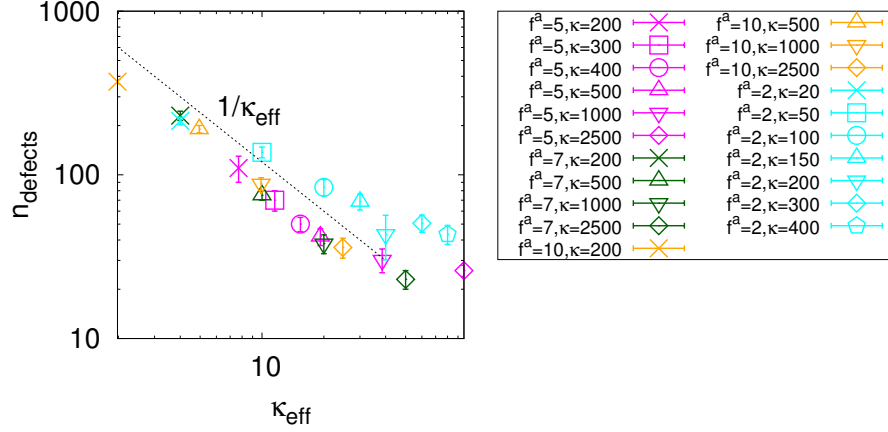


FIG. S1. Number of defects as a function of κ_{eff} for the alternative dataset, with FENE bond strength $k_b = 30$ and active reversal period, $\tau_1 = 1$. Notice that we observe data collapse for all parameters with $f^a \geq 5$, but not for the lowest activity $f^a = 2$ (light blue symbols), when the system begins to lose nematic order (see Fig. S5c below) and the active force strength becomes comparable to thermal forces.

S4. ESTIMATING THE INDIVIDUAL FILAMENT PERSISTENCE LENGTH

In this section we describe estimates of the effective persistence length measured from the tangent fluctuations of individual filaments. We performed these measurements both on individual filaments within a bulk active nematic, and isolated individual filaments to distinguish single-chain and multi-chain effects on the effective persistence length.

In a continuum limit, the total bending energy of a semiflexible filament it is well approximated by the wormlike chain model [2],

$$H_{\text{bend}} = \frac{\tilde{\kappa}}{2} \int_0^L \left(\frac{d\theta}{ds} \right)^2 ds \quad (\text{S1})$$

where the integration is over the filament contour length, L , parameterized by s , $\tilde{\kappa}$ is the continuum bending modulus, and $\theta(s)$ is the tangent angle along the contour.

For a normal-mode analysis of the bending excitations we performed a Fourier decomposition of the tangential angle $\theta(s)$ assuming general boundary conditions (since a filament in bulk need not be force-free at its ends):

$$\theta(s) = \sum_q (a_q \cos(qs) + b_q \sin(qs)) \quad (\text{S2})$$

where $q = n\pi/L$ ($n = 1, 2, 3, \dots$) is the wave vector, with corresponding wavelength $\lambda = \pi/q$.

At equilibrium, using Eqs. (S1) and (S2) along with the equipartition theorem results in

$$\langle a_q^2 + b_q^2 \rangle = \frac{2k_B T}{\tilde{\kappa} L q^2}. \quad (\text{S3})$$

The modulus $\tilde{\kappa}$ can then be estimated from the slope of $\langle a_q^2 + b_q^2 \rangle$ vs. q , as shown for an example parameter set in Fig. S2, and the persistence length is given by $l_p = \tilde{\kappa}/k_B T$. Performing this procedure for our non-equilibrium system as a function of κ and f^a allows estimating the effective filament persistence length (Fig. 3 main text).

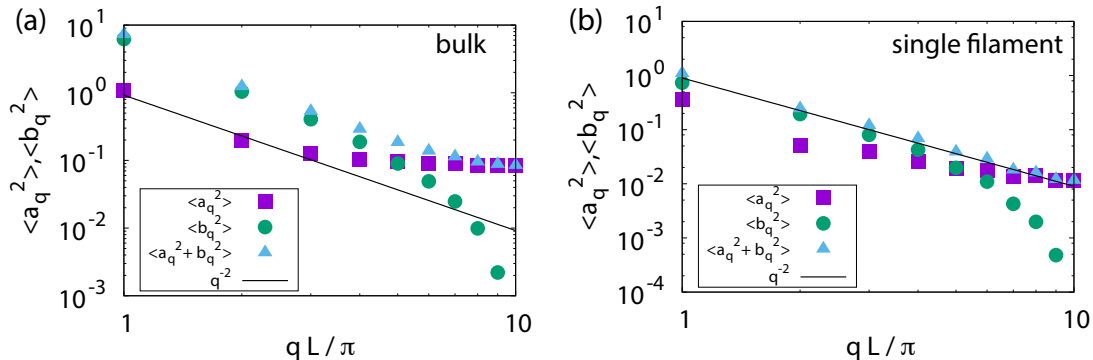


FIG. S2. Fourier amplitudes $\langle a_q^2 \rangle$, $\langle b_q^2 \rangle$ and $\langle a_q^2 + b_q^2 \rangle$ as a function of wave vector qL/π , with $L = bM$ the filament contour length, measured in simulations of (a) bulk active nematics and (b) an isolated filament, for representative parameter values ($\kappa = 500, f^a = 10; \kappa_{\text{eff}} = 5$). Other parameters are $\tau_1 = \tau$ and $k_b = 30k_B T_{\text{ref}}/\sigma^2$.

S5. SPLAY AND BEND DEFORMATIONS

In a continuum description of a 2D nematic, all elastic deformations can be decomposed into bend and splay modes, given by $\mathbf{d}_{\text{bend}}(\mathbf{r}) = (\hat{n}(\mathbf{r}) \times (\nabla \times \hat{n}(\mathbf{r})))$ and $d_{\text{splay}}(\mathbf{r}) = (\nabla \cdot \hat{n}(\mathbf{r}))$. Fig. S3 shows the spatial distribution of bend and splay deformations in systems at low and high rigidity values. To avoid breakdown of these definitions within defect cores or other vacant regions, we have normalized the deformations by the local density and nematic order: $D_{\text{bend}} = \rho S^2 |\mathbf{d}_{\text{bend}}|^2$ and $D_{\text{splay}} = \rho S^2 d_{\text{splay}}^2$. We see that bend and splay are equally spread out in the system in the limit of low rigidity, whereas bend deformations are primarily located near defect cores for large rigidity. In the high rigidity simulations, the effective persistence length ($\approx 66\sigma$) significantly exceeds the filament contour length (20σ), and thus most bend deformations correspond to rotation of the director field around filament ends at a defect tip.

To obtain further insight into the spatial organization of deformations, we calculated power spectra as $P_k^{\text{bend}} = \int d^2\mathbf{r}' \exp(-i\mathbf{k} \cdot (\mathbf{r}')) \langle D_{\text{bend}}(\mathbf{r}) D_{\text{bend}}(\mathbf{r} + \mathbf{r}') \rangle$, with an analogous definition for splay, and with the Q field calculated at 1000×1000 grid points (a realspace gridspacing of 0.84σ). The resulting power spectra are shown in Fig. S4a,b as functions of the renormalized filament rigidity, and the dependences of the peak positions and maximal power are discussed in the main text. Here we note that the splay spectra exhibit asymptotic scaling of $k^{5/3}$ and $k^{-8/3}$ at scales respectively above the defect spacing or below the size of individual filaments, with a plateau region at intermediate scales. The same asymptotic scalings in power spectra were observed in dense bacterial suspensions in the turbulent regime [3, 4].

The main text discusses the ratio of total strain energy in splay deformations to those in bend

$$R = \left\langle \int d^2\mathbf{r} D_{\text{splay}}(\mathbf{r}) \right\rangle / \left\langle \int d^2\mathbf{r} D_{\text{bend}}(\mathbf{r}) \right\rangle. \quad (\text{S4})$$

We find that this ratio scales as $R \sim \kappa_{\text{eff}}^{1/2}$ for all parameter sets, which is different from the expected scaling in an equilibrium nematic of $R_{\text{eq}} \sim \kappa^{2/3}$. To investigate the origins of this discrepancy, we measured the elastic moduli for an equilibrium system for different κ values shown in Fig. (S5). We find that the degree of order in the system depends on the value of κ , that approximate scalings can be identified as $k_{33} \sim S^4$ and $k_{11} \sim S^2$ (Fig. (S5b)), and that the amount of order in the system at a given stiffness value κ_{eff} is very different for active nematics when compared to their equilibrium analogs (Fig. (S5c)). Active nematics have considerably higher order. We used this information to empirically find that R/S^2 exhibits approximately the same scaling for active and passive nematics.

Finally, by analogy to equipartition at equilibrium, the ratio of splay/bend, R , can be construed as an effective ratio of moduli: $k_{33}^{\text{effective}}/k_{11}^{\text{effective}}$, with the ratio depending on activity. Fig. S6 shows the defect shape parameter plotted as a function of this ratio.

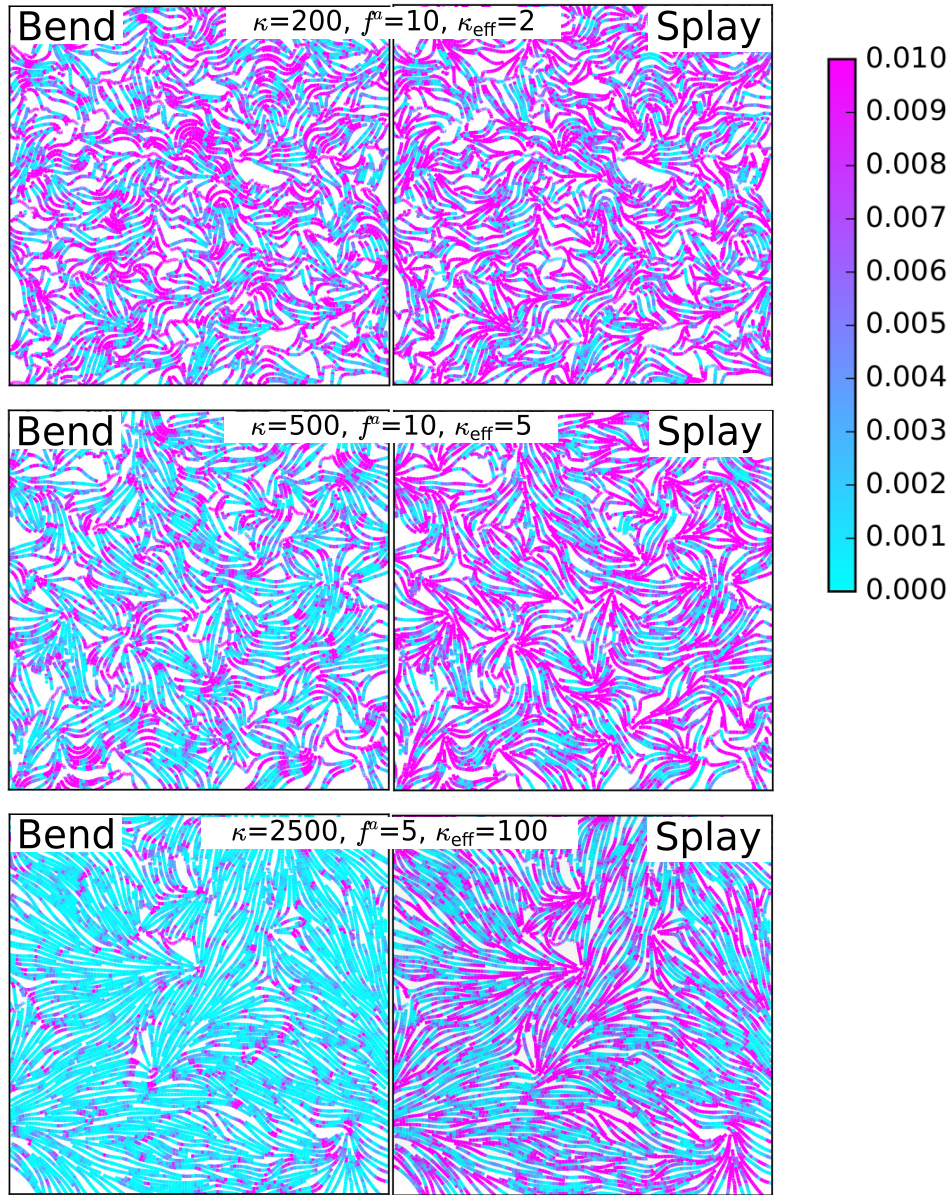


FIG. S3. Snapshots from steady state configurations at indicated parameter values, with colormaps showing the distribution of bend, $\rho S^2(\hat{n} \times (\nabla \times \hat{n}))^2$ (left), and splay, $\rho S^2(\nabla \cdot \hat{n})^2$ (right), superposed on lines representing the director field. The parameters are chosen to highlight differences between flexible (small κ_{eff}) and rigid (large κ_{eff}) systems. The color range is clipped at 0.01 to clarify the spatial variations of the deformations. Other parameters are $\tau_1 = 0.2\tau$ and $k_b = 300k_B T_{\text{ref}}/\sigma^2$.

S6. SYSTEM SIZE EFFECTS

To assess finite size effects on our results, we performed a system size analysis for two parameter sets from Fig. S1: $\kappa = 200, f^a = 5$ and $\kappa = 2500, f^a = 5$, with $\tau_1 = \tau$ and $k_b = 30$. We chose these parameter sets because they are near the upper and lower limits of effective bending rigidity investigated in that set of simulations. As shown in Fig. S7, we observe no systematic dependence of defect density on system size over the range of side lengths $L \in [200, 1200]\sigma$. We observe a similar lack of dependence on system size for other observables, suggesting that finite size effects are negligible in our simulations at system size $(840 \times 840\sigma^2)$.

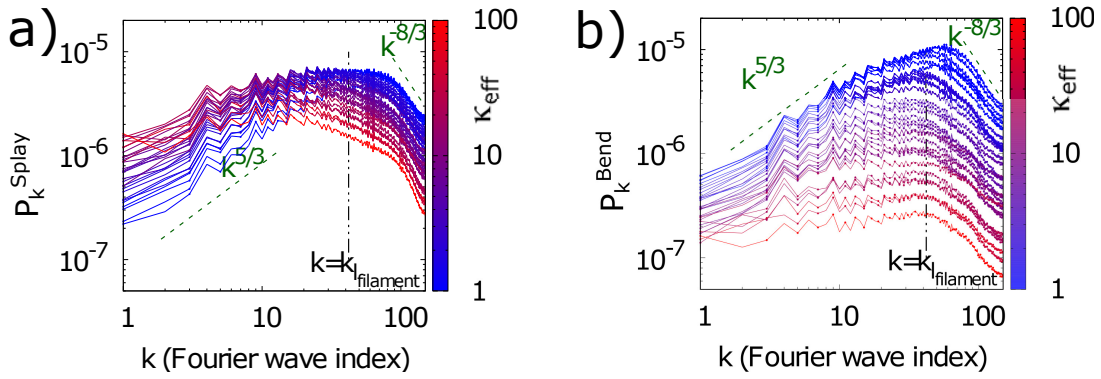


FIG. S4. Power spectrum of splay (a) and bend (b) deformations as a function of wavenumber k , with the colorbar indicating the value of effective bending rigidity (κ_{eff}). Other parameters are $\tau_1 = 0.2\tau$ and $k_b = 300k_B T_{\text{ref}}/\sigma^2$.

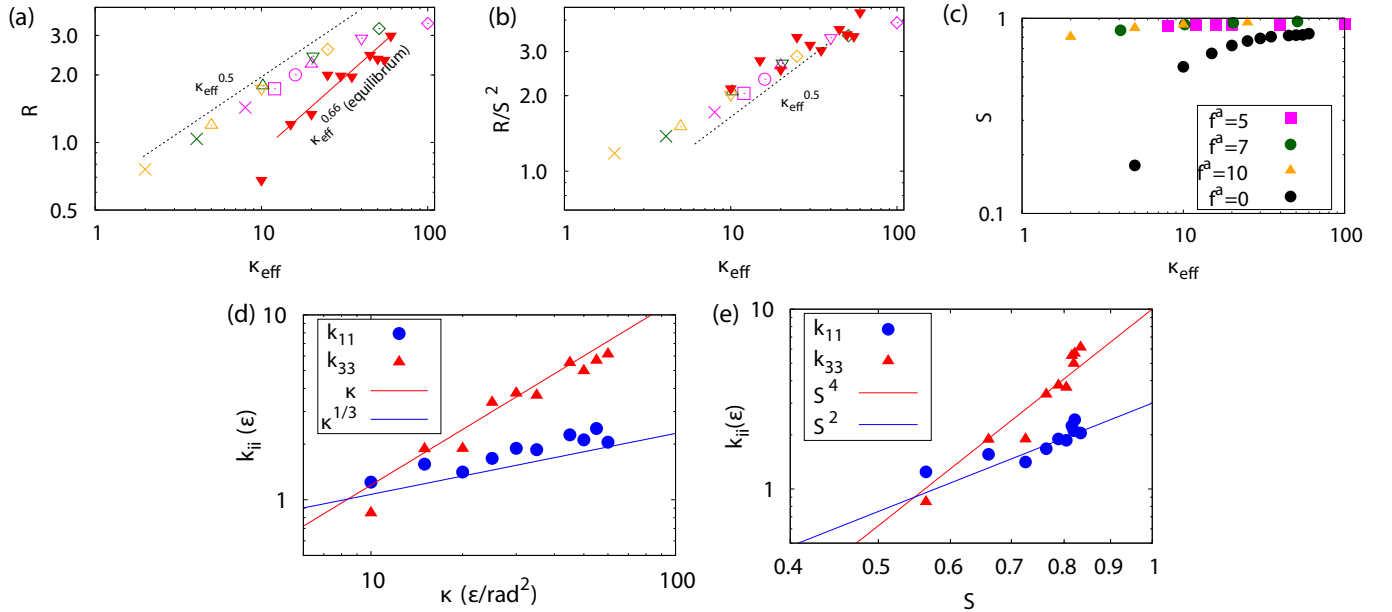


FIG. S5. Comparison of ratio of bend and splay deformations in an active nematic to an equilibrium system. (a) The ratio of splay and bend deformations, R , plotted as a function of renormalized bending rigidity for active and equilibrium systems. The ratio R calculated in equilibrium systems is shown as \blacktriangledown symbols, while the symbols for the active system are defined as in Fig. S1. (b) The data from (a) is shown normalized by the mean nematic order parameter squared, (R/S^2) . (c) The mean nematic order parameter, S , as a function of renormalized bending rigidity measured in active and equilibrium simulations. (d) Values of the bend (k_{33}) and splay (k_{11}) elastic constants as a function of κ calculated using free energy perturbation [1] in equilibrium simulations ($f^a = 0$). (e) The same results as in (d), plotted against the nematic order parameter S calculated for each parameter value. The red and blue lines indicate scaling of $\sim S^4$ and $\sim S^2$. The active results in this figure correspond to the additional data set with $k_b = 30$ and $\tau_1 = 1$, as in Fig. S1.

S7. DENSITY FLUCTUATIONS

It is well-known that active nematics are susceptible to phase separation [5–8] and giant number fluctuations (GNFs) [5, 9–12]. We therefore monitored these quantities in our system. Interestingly, while we do observe large density fluctuations on small scales (see videos of typical trajectories), phase separation is suppressed on large scales in the semiflexible regime. Fig. S8 shows histograms of local density, measured within subsystems with side length 10σ as a function of κ . We see that the distribution of local densities broadens as f^a and κ increase, but remains unimodal indicating an absence of true phase separation.

Fig. S9 shows measured number fluctuations for different values of the effective bending modulus, plotted as $\Delta N/\sqrt{N}$, so that the result will be constant with subsystem size for a system exhibiting equilibrium-like fluctuations.

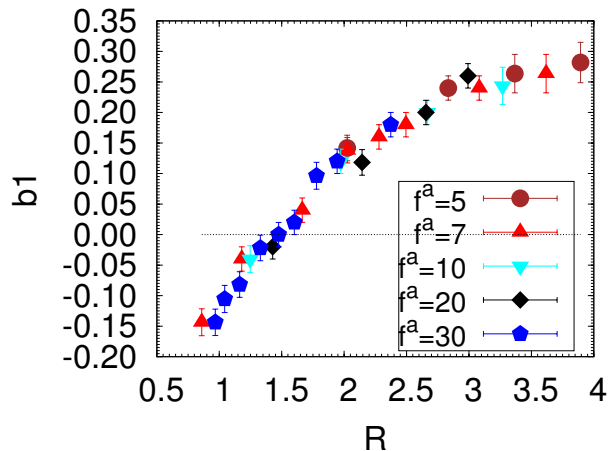


FIG. S6. Defect shape parameter b_1 as a function of splay/bend ratio R defined in the text, for the data in Fig. 3b,c of the main text.

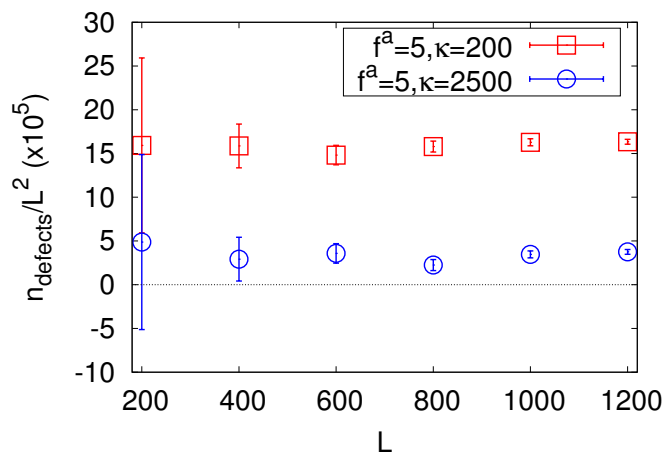


FIG. S7. Steady-state defect density as a function of simulation box side length L for square boxes with periodic boundary conditions, at indicated values of the filament modulus and activity parameter, with $\tau_1 = \tau$ and $k_b = 30k_B T_{ref}$.

S8. DEFECT IDENTIFICATION AND SHAPE MEASUREMENT ALGORITHM

Here, we provide details on how we identify and measure the shapes of defects from our simulation data. This algorithm can also be directly applied to retardance images from experimental systems, and discretized output from continuum simulations.

Locating and identifying defects: We locate defects using the fact the magnitude of nematic order S is very small at defect cores. We first compute the magnitude $S = 2\sqrt{Q_{xx}^2 + Q_{xy}^2}$ from the nematic tensor, whose measurement was described above. The regions corresponding to defect cores can then be extracted by using a flood-fill algorithm to select connected areas where the order is below some threshold $S_{\text{threshold}}$. We set $S_{\text{threshold}} = 0.6$ since the system is deep within the nematic state for the parameters of this study. Once the defect cores have been located, the charge of each defect can be identified from the total change in the orientation of the director in a loop around the defect core. We perform this calculation by adding the change in angle for points in a circle about the center of the core. We choose the radius of the circle to be at least 5σ , to ensure a well defined director field. The total change in angle must be a multiple of π : $\Delta\theta = n\pi$, where if $n = 0$ then the disordered region is not a defect, and otherwise it is a defect with topological charge $m = \frac{n}{2}$. Typically $n = \pm 1$ but, in rare cases we observed defects with charge $m = +1$ in our simulation data.

Identifying the orientations and characterizing the shapes of $+\frac{1}{2}$ defects: Given the location of a defect and its

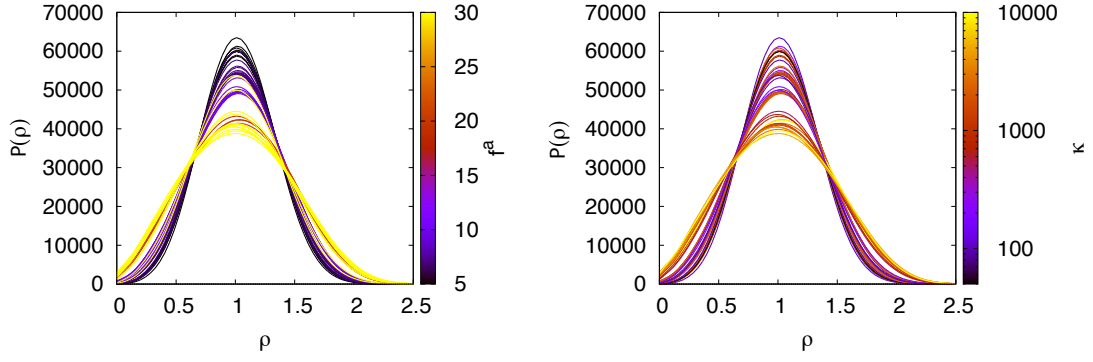


FIG. S8. The distribution of local densities of filament pseudoatoms for indicated values of activity (**left**) and bare bending rigidity (**right**). Local densities were calculated by measuring the number of filament beads within square subsystems with side length 10σ . Other parameters are $\tau_1 = 0.2\tau$ and $k_b = 300k_B T_{\text{ref}}/\sigma^2$.

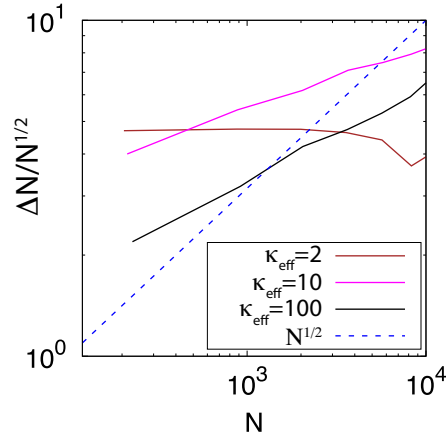


FIG. S9. Giant number fluctuations (GNFs) depend on the renormalized bending rigidity. (**a**). The mean fluctuations of number of filament pseudoatoms, ΔN , is plotted as a function of subsystem size N for representative values of κ_{eff} . The fluctuations are normalized by their value at equilibrium, $\Delta N/\sqrt{N}$ so that a horizontal line indicates equilibrium-like fluctuations. Other parameters are $\tau_1 = 0.2\tau$ and $k_b = 300k_B T_{\text{ref}}/\sigma^2$.

charge, there are several methods which can be used to measure the orientation of the $+\frac{1}{2}$ defects [13, 14]. In this work, we compute the sum of the divergence of \mathbf{Q} field, $\nabla_\beta Q_{\alpha\beta}$ along a circle enclosing the defect, and normalize it to a give unit vector. This unit vector represents the orientation of the $+1/2$ defect and in our two dimensional system identifies an angle θ'_0 for the defect.

We then measure the director orientation $\bar{\theta}(\bar{\phi})$ along the azimuthal angle $\bar{\phi}$ at discrete set of radii, $\{r\}$, around the defect core (see Fig. 5A main text). First, we ensure that each loop does not cross any disordered regions, or enclose any other defects, by checking the order at each point and summing $\Delta\theta$ over the loop. Then we apply a coordinate frame rotation such that $\theta = \bar{\theta} - \theta'_0$, and the azimuthal angle $\phi = \bar{\phi} - \theta'_0$, where, θ'_0 is an orientation of the $+1/2$ defect estimated above. This step rotates the coordinate frame of reference to the frame of reference of the $+1/2$ defect. Finally, we evaluate the Fourier coefficients for $\theta(\phi)$,

$$\theta(r, \phi) = +\frac{1}{2}\phi + \sum_n a_n(r) \cos(n\phi) + b_n(r) \sin(n\phi). \quad (\text{S5})$$

However, in practice we find that truncating the expansion after the first sin term gives an excellent approximation of the shape of a $+\frac{1}{2}$ defect. Hence, once a value of r is chosen, the defect can be characterized by the single parameter b_1 .

In Fig. S10 we show the distribution of b_1 values obtained from our simulations with $r = 12.6\sigma$. Note that we observe long tailed distributions of b_1 with tails in the $b_1 < 0$ regime. However, the distributions are sharply peaked with typical peak width ~ 0.1 . Therefore we consider the mode of b_1 values as an appropriate measure of defect shape.

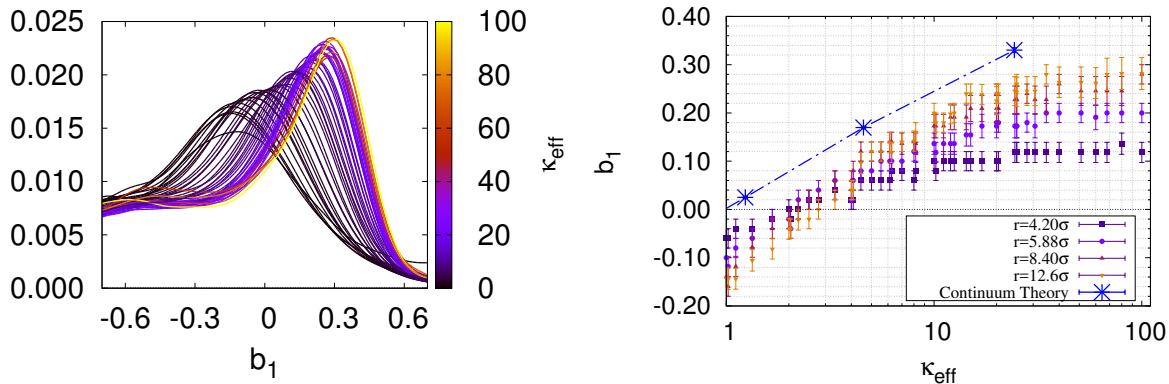


FIG. S10. **(left)** Normalized distributions of b_1 obtained from the simulations with $\tau_1 = 0.2\tau$ and $k_b = 300k_B T_{\text{ref}}/\sigma^2$, with parameterizations calculated at a distance $r = 12.6\sigma$ from the center of each defect according to Eq. (S5). **(right)** Effect of varying r (the distance from the center of the $+1/2$ defect core) on the defect shape parameter b_1 . The mode of b_1 is shown as a function of κ_{eff} for the simulations in Fig. 3 (main text), with indicated values of r .

Choice of r : For an isolated defect, b_1 asymptotes once the distance from the defect center increases beyond the core size. However, as noted in Zhou et al. [15], in a system with finite defect density the defect shape should be parameterized as close to the defect center as possible to avoid distortion due to other defects. The typical defect core radius in our simulations (defined as the region in which the nematic order parameter $S < 0.6$) is about 4σ . The smallest defect spacing (at the highest defect density) in our simulations is about 40σ . We therefore chose a radius $r = 12.6\sigma$, where the nematic is highly ordered and the director is always well-defined, but distortions due to other defects are minimized. As shown in Fig. S10 (right) the results are qualitatively insensitive to radius for $r > 5$, although statistics become more limited for larger r . For consistency, the same radius should be chosen for all systems.

Breakdown at high f^a and κ : As noted in the main text, the defect identification algorithm breaks down in systems with both extremely high activity and high bare bending rigidity ($f^a \geq 20$ and $\kappa \gtrsim 5000$). Under these conditions the system exhibits density fluctuations on very short length scales (see Fig. S8 and the movie showing snapshots from a simulation trajectory with $f^a = 30$ and $\kappa = 10^4$). The defect algorithm cannot distinguish between configurations in which stiff rods trans-pierced these holes and actual defects. Therefore we have not measured defect densities for these parameter sets.

-
- [1] A. A. Joshi, J. K. Whitmer, O. Guzmán, N. L. Abbott, and J. J. de Pablo, *Soft Matter* **10**, 882 (2014).
[2] M. Doi and S. Edwards, *The Theory of Polymer Dynamics*, International series of monographs on physics (Clarendon Press, 1988).
[3] H. H. Wensink, J. Dunkel, S. Heidenreich, K. Drescher, R. E. Goldstein, H. Lowen, and J. M. Yeomans, *Proc. Nat. Acad. Sci. U.S.A.* **109**, 14308 (2012), 1208.4239v1.
[4] R. Chatterjee, A. A. Joshi, and P. Perlekar, *Phys. Rev. E* **94**, 022406 (2016), arXiv:1608.01142.
[5] S. Mishra and S. Ramaswamy, *Phys. Rev. Lett.* **97**, 090602 (2006).
[6] S. Ngo, A. Peshkov, I. S. Aranson, E. Bertin, F. Ginelli, and H. Chaté, *Phys. Rev. Lett.* **113**, 038302 (2014), arXiv:1312.1076.
[7] E. Putzig and A. Baskaran, *Phys. Rev. E* **90**, 042304 (2014), 1057984.
[8] X.-q. Shi and Y.-q. Ma, *Nat. Comm.* **4**, 3013 (2013).
[9] S. Ramaswamy, R. A. Simha, and J. Toner, *Europhys. Lett.* **62**, 196 (2003).
[10] H. Chaté, F. Ginelli, and R. Montagne, *Phys. Rev. Lett* **96**, 180602 (2006).
[11] V. Narayan, S. Ramaswamy, and N. Menon, *Science* **317**, 105 (2007).
[12] H. P. Zhang, A. Be'er, E.-L. Florin, and H. L. Swinney, *Proc. Natl. Acad. Sci. U. S. A.* **107**, 13626 (2010), <http://www.pnas.org/content/107/31/13626.full.pdf>.
[13] S. J. DeCamp, G. S. Redner, A. Baskaran, M. F. Hagan, and Z. Dogic, *Nat. Mater.* **14**, 1110 (2015).
[14] A. J. Vromans and L. Giomi, *Soft Matter* , 1 (2015), 1507.05588.
[15] S. Zhou, S. V. Shiyantovskii, H.-S. Park, and O. D. Lavrentovich, *Nat. Commun.* **8**, 14974 (2017).